

Spectral control over γ -ray echo using a nuclear frequency comb system

Chia-Jung Yeh,¹ Po-Han Lin,¹ Xiwen Zhang,² Olga Kocharovskaya,³ and Wen-Te Liao^{1,*}

¹*Department of Physics, National Central University, Taoyuan City 32001, Taiwan*

²*Department of Physics and Astronomy, University of Toronto, Toronto, Ontario M5S 1A7, Canada*

³*Department of Physics and Astronomy, Texas A&M University, College Station, Texas 77843, USA*

(Dated: July 8, 2019)

Two kinds of spectral control over γ -ray echo using a nuclear frequency comb system are theoretically investigated. A nuclear frequency comb system is composed of multiple nuclear targets under magnetization (hyperfine splitting), mechanical motion (Doppler shift) or both, namely, moving and magnetized targets. In frequency domain the unperturbed single absorption line of γ -ray therefore splits into multiple lines with equal spacing and becomes a nuclear frequency comb structure. We introduce spectral shaping and dynamical splitting to the frequency comb structure respectively to optimize the use of a medium and to break the theoretical maximum of echo efficiency, i.e., 54%. Spectral shaping scheme leads to the reduction of required sample resonant thickness for achieving high echo efficiency of especially a broadband input. Dynamical splitting method significantly advances the echo efficiency up to 67% revealed by two equivalent nuclear frequency comb systems. We also show that using only few targets is enough to obtain good echo performance, which significantly eases the complexity of implementation. Our results extend quantum optics to 10keV regime and lay the foundation of the development of γ -ray memory.

Keywords:

The γ -ray-nuclear interfaces are recently demonstrated to be interesting for fundamental physics in the development of γ -ray/X-ray quantum optics [1], which explores a completely new energy realm of light-matter interactions [2–16]. Pursuing coherent control over γ -rays is also expected to be versatile for applications [17–23]. E.g., spectral control over γ -rays may lead to new light source for Mössbauer spectroscopy [21]. Given the sub-angstrom wavelength of γ -photon, it avoids the bottleneck of diffraction limit for photonic information processing [17, 24], e.g., γ -photon storage [24–27]. γ -ray echo [28, 29] is shown to be a valuable and practical method for shaping γ -ray wavepacket [17] and forming nuclear quantum memory [27]. In this letter, we put forward spectral shaping and dynamical splitting to manipulate the recently proposed nuclear frequency comb (NFC) [27] and its resulting γ -ray echo. The former is used to optimize the echo efficiency, and the latter is intended for beating the theoretically maximum echo efficiency of 54% [27, 30]. In view of the success of the optical echo memory [30–36] based on atomic frequency comb (AFC) [37, 38], our scheme gives an important step for the development of future γ -ray echo memory [27]. Moreover, the present results suggest applications such as a γ -ray coherent delay line providing an input γ -ray pulse with a tunable time delay, and the generation of time-bin qubit for single γ quanta.

We begin with the optimization of a NFC using spectral shaping. Figure 1(a) illustrates our modified NFC system by introducing a resonant thickness distribution function $P(\Delta)$ to a sequence of targets. The spatial order of the comb teeth does not matter. The energy shift Δ from the unperturbed transition energy can be generated by, e.g., Doppler shift, and the afterimage of each cuboid depicts its motion with a constant velocity [27]. The coloured cuboids represent targets where embedded nuclei experience different Δ . With a proper arrangement, multiple absorption peaks can form a NFC with a tunable comb spacing $S\Gamma$. Here Γ is the spontaneous de-

cay rate of some chosen excited states, and $S > 0$. Red, orange, yellow, green and blue are respectively for $\Delta = -2S\Gamma$, $-S\Gamma$, zero, $S\Gamma$ and $2S\Gamma$. The yellow short pulse depicts the incident γ -ray. Since the absorption strength is proportional to resonant thickness, $P(\Delta)$ modifies the overall NFC in the frequency domain as depicted in Fig. 1(b). The black-solid-yellow-filled line demonstrates the spectrum of the incident γ -ray pulse. In view that the input spectral intensity on res-

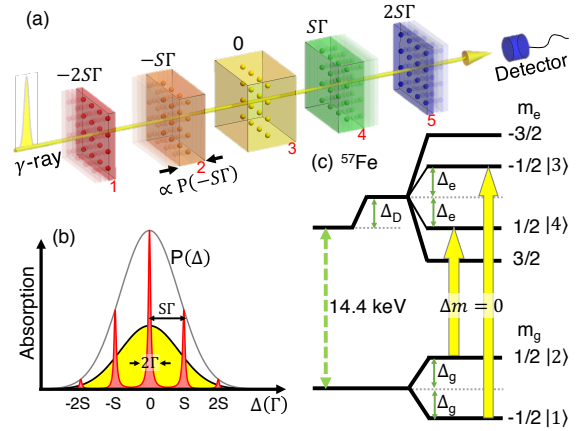


FIG. 1: (Color online) (a) nuclear frequency comb system made of multiple targets with a resonant thickness distribution $P(\Delta)$. Cuboid of each color depicts nuclei in which experience an energy shift specified above cuboid, e.g., red for a shift of $-2S\Gamma$ from unperturbed transition energy. (b) spectral shaping of a nuclear frequency comb by introducing $P(\Delta)$. Nuclear frequency comb with equal spacing $S\Gamma$ formed by nuclear absorption lines of different targets, and each linewidth is 2Γ . (c) ^{57}Fe nuclear level scheme. A linearly polarized γ -ray (yellow-upward-wide arrows) drives $\Delta m = 0$ transitions. Δ_g (Δ_e) is the ground (excited) state hyperfine splitting, and Δ_D is the Doppler shift. The situation when both $\Delta_D \neq 0$ and $\Delta_g + \Delta_e \neq 0$ is termed as hybrid shift.

onance with unperturbed transition is stronger than those at side bands, $P(\Delta)$ can properly match the overall NFC (multiple red-solid-filled peaks) with the input spectrum such that the use of whole medium is optimal. This will ease the demand of very high resonant thickness for achieving high echo efficiency in a flat comb [27].

Figure 1(c) shows the level scheme of ^{57}Fe nucleus with hyperfine splitting $\Delta_g + \Delta_e$ and Doppler shift Δ_D . Without Doppler shift, i.e., $\Delta_D = 0$, multiple magnetized and stationary targets can also form a NFC when $\Delta_g + \Delta_e = S\Gamma$, and each target contributes a pair of comb tooth for a linearly polarized γ -ray. For the sake of simplicity we term the case when both $\Delta_D \neq 0$ and $\Delta_g + \Delta_e \neq 0$ as hybrid shift. The Maxwell-Bloch equation for the n th target in perturbation regime [24, 35, 39, 40], namely, $|\Omega_n| \ll \Gamma$, describes the coupling between nuclei and γ -ray:

$$\partial_t \rho_{31}^n = - \left[\frac{\Gamma}{2} + i\Delta_{31}^n(t) \right] \rho_{31}^n + i\frac{a}{4}\Omega_n, \quad (1)$$

$$\partial_t \rho_{42}^n = - \left[\frac{\Gamma}{2} + i\Delta_{42}^n(t) \right] \rho_{42}^n + i\frac{a}{4}\Omega_n, \quad (2)$$

$$\frac{1}{c}\partial_t \Omega_n + \partial_z \Omega_n = i\eta_n a (\rho_{31}^n + \rho_{42}^n). \quad (3)$$

Together with initial conditions $\rho_{31}^n(0, z) = \rho_{42}^n(0, z) = 0$, $\Omega_n(0, z) = 0$ and the input boundary condition $\Omega_1(t, 0) = \Omega_0 \text{Exp} \left[- (t - \tau_i)^2 / \tau_p^2 \right]$. Other boundary conditions are $\Omega_{n>1}(t, 0) = \Omega_{n-1}(t, L_{n-1})$, i.e., we treat the output from $(n-1)$ th target as the input of n th target. Here ρ_{31}^n and ρ_{42}^n are the slowly varying amplitudes of the coherence term in the density matrix of the level scheme illustrated in Fig. 1(c). Ω_n is the slowly varying amplitudes of the Rabi frequency of the linearly polarized γ -ray propagating through n th target, and c represents the speed of light. Above mentioned Δ is generalized for ^{57}Fe nuclear hyperfine structure. Energy shift of transition $|1\rangle \rightarrow |3\rangle$ and $|2\rangle \rightarrow |4\rangle$ are respectively $\Delta_{31}^n = \Delta_g^n + \Delta_e^n + \Delta_D^n$ and $\Delta_{42}^n = -(\Delta_g^n + \Delta_e^n) + \Delta_D^n$. The coupling con-

stant $\eta_n = 6\Gamma\xi_n/L_n$, where $\Gamma = 1/141.1$ GHz is the spontaneous decay rate of excited states $|3\rangle$ and $|4\rangle$, ξ_n the resonant thickness and L_n the thickness of n th target. $a = \sqrt{2/3}$ is the corresponding Clebsch-Gordan coefficient for two $\Delta m = m_e - m_g = 0$ transitions in Fig. 1(c). For flat NFC, a Fourier analysis [27, 41] of Eq. (1-3) shows that the echo efficiency $\mathbb{E} = \left[\int_{t_1}^{t_2} |\Omega_M(t, L_M)|^2 dt \right] / \left[\int_{-\infty}^{\infty} |\Omega_1(t, 0)|^2 dt \right] = 16\pi^2 \bar{\xi}^2 \text{Exp} \left[-2\pi(2\bar{\xi} + 1)/S \right] / S^2$ where $\bar{\xi} = \sum_{n=1}^M \xi_n / M$ is the average resonant thickness over total M targets. Temporal domain $[t_1, t_2]$ contains only echo signal which peaks at $\tau_e = \tau_i + 2\pi/(S\Gamma)$. The theoretical maximum \mathbb{E} is 54% when $\bar{\xi}$ and S approach infinity as also predicted by typical echo memory system limited by re-absorption [30, 41]. While the required target parameters are not realistic for $\mathbb{E} = 54\%$, we would like to address the question of how to achieve reasonably high \mathbb{E} with an optimization of resonant thickness? As a reference a flat comb with $(S, \bar{\xi}) = (50, 8)$ results in $\mathbb{E} = 47.7\%$.

In order to match NFC and the spectrum of an input Gaussian pulse, we let ξ_n proportional to a normalized Gaussian distribution

$$P(n, k) = \frac{\text{Exp} \left\{ - \left[\frac{1}{2} k \tau_p \left(n - \frac{M+1}{2} \right) S \Gamma \right]^2 \right\}}{\sum_{m=1}^M \text{Exp} \left\{ - \left[\frac{1}{2} k \tau_p \left(m - \frac{M+1}{2} \right) S \Gamma \right]^2 \right\}}, \quad (4)$$

where the total target number $M \in \text{odd}$. This spectral shaping can be achieved by controlling either the isotope concentration or the target thickness during crystal growth. The modified comb structure in Fig. 1(b) is given by multiplying the flat comb [27] and $P(n, k)$, where parameter k is used to adjust the overall width of NFC, e.g., $k = 0$ for a flat comb and $k = 1$ for a NFC width equals to the bandwidth of the incident pulse. The analytical solution of the output signal due to spectral shaping reads (see Supplementary Material for derivation)

$$\Omega_M(t, L_M) = \frac{\Omega_0 \sqrt{\pi} \tau_p}{2T} \sum_{l=-\infty}^{\infty} \text{Exp} \left[- \left(\frac{l\pi\tau_p}{2T} \right)^2 + il\pi \frac{t - \tau_i}{T} - 2i\xi\Gamma \sum_{n=1}^M \frac{P(n, k)}{-l\frac{\pi}{T} - \left(n - \frac{M+1}{2} \right) S\Gamma + i\frac{\Gamma}{2}} \right], \quad (5)$$

where $\xi = M\bar{\xi} = \sum_{n=1}^M \xi_n$ is the total resonant thickness, and the introduced T must be long enough to cover the complete output signal.

The consistency between Eq. (5) and numerical solution has been carefully checked (see Supplementary Material). Fig. 2 shows the (k, ξ) -dependent echo efficiency based in Eq. (5) and demonstrates the general effect of spectral shaping technique. An unperturbed single target can be utilized to control only a tiny Fourier fraction of a broadband input pulse whose bandwidth is much larger than the natural linewidth of

the absorber. The use of very high ξ may ease the broadband difficulty but will degrade \mathbb{E} due to dispersion [35]. Spectral shaping technique in NFC will lower the needed ξ and provides a solution to above problem. In Fig. 2(a) we demonstrate a broadband echo efficiency by using $(\tau_p, S, M) = (1\text{ns}, 50, 21)$, i.e., an input bandwidth of 141Γ . It plainly exhibits, on one hand, the k -dependent improvement of \mathbb{E} , e.g., \mathbb{E} is prominently raised from 30% to 44% when $k = 1$ is introduced for $\xi = 80$. On the other hand, the k -induced reduction of needed ξ for achieving some \mathbb{E} can be observed for

all contours. Fig. 2(b) shows another prominent example for $(\tau_p, S, M) = (5\text{ns}, 50, 9)$, namely, a narrower input bandwidth of 28Γ . The required ξ for $\mathbb{E} > 50\%$ significantly decreases from 60 for $k = 0$ to 26 for $k = 0.5$. One can see that $P(n, k > 0)$ -modified NFC not only preserves the echo performance but also offers the advantage of the reduction of required ξ . Comparing shaped NFC with flat comb, maximum 22% and 53% reduction of ξ are observed for $\tau_p = 1\text{ns}$ and $\tau_p = 5\text{ns}$, respectively, whose parameters are indicated by green dot, black cross, brown-filled square and blue cross in Fig. 2(a) and Fig. 2(b). The $P(n, k)$ -modified NFC therefore optimizes the use of resonant thickness in contrast to a flat comb. In view of Fig. 1(b), \mathbb{E} of a narrow band input is mainly determined by the central resonant line and $\Delta = \pm ST$ side bands, because the spectral intensity of incident photons in this range is high. Including high order side bands mainly leads to even higher \mathbb{F} because more frequency components are involved in the re-phasing process. One can therefore remove targets contributing $\Delta > ST$ side bands with negligible change in \mathbb{E} . Along this line, in Fig. 2(c) we discuss the reduction of target number M via finding maximum \mathbb{E} in the domain of $0 \leq \bar{\xi} \leq 15$ for each M , and calculate the corresponding fidelity \mathbb{F} [27, 35, 42], where

$$\mathbb{F} = \frac{|\int_{t_1}^{t_2} \Omega_1^*(t - \tau_e, 0) \Omega_M(t, L) dt|^2}{\left[\int_{-\infty}^{\infty} |\Omega_1(t, 0)|^2 dt \right] \left[\int_{t_1}^{t_2} |\Omega_M(t, L)|^2 dt \right]}.$$

Brown-filled squares and green dots respectively depict M -dependent maximum \mathbb{E} for $\tau_p = 5\text{ns}$ and for $\tau_p = 1\text{ns}$ using flat comb ($k = 0$). Orange squares and red circles are their fidelity. The 5ns echo performance already reaches $\mathbb{E} = 51\%$ and $\mathbb{F} = 99\%$ as $M = 3$. However, more targets ($M > 11$)

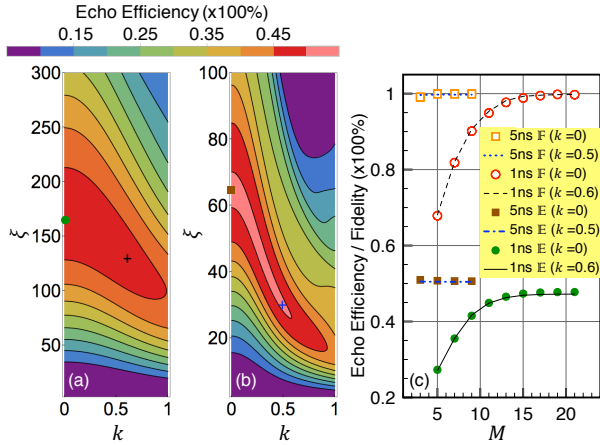


FIG. 2: (Color online) (k, ξ) -dependent echo efficiency \mathbb{E} based in an analytical solution Eq. (5) for (a) $(\tau_p, S, M) = (1\text{ns}, 50, 21)$ and (b) $(\tau_p, S, M) = (5\text{ns}, 50, 9)$. Green dot, black cross, brown-filled square and blue cross indicate the parameter sets $(k, \xi, M) = (0, 166, 21)$, $(0.6, 129, 21)$, $(0, 64, 9)$ and $(0.5, 30, 9)$, respectively, used in (c) to show the reduction of total resonant thickness due to spectral shaping. (c) M -dependant \mathbb{E} and fidelity \mathbb{F} . For $\tau_p = 5\text{ns}$, orange squares and brown-filled squares (blue-dotted line and blue-dashed-dotted line) respectively depict \mathbb{F} and \mathbb{E} for $k = 0$ ($k = 0.5$). For $\tau_p = 1\text{ns}$, red circles and green dots (black-dashed line and black-solid line) respectively illustrate \mathbb{F} and \mathbb{E} for $k = 0$ ($k = 0.6$).

are needed for $\tau_p = 1\text{ns}$ to achieve $\mathbb{E} > 47\%$ and $\mathbb{F} > 97\%$ due to its larger bandwidth than both Γ and comb spacing. To manifest the advantage of spectral shaping technique, we show another set of \mathbb{E} and \mathbb{F} for $\tau_p = 1\text{ns}$ using $k = 0.6$ with black-solid line and black-dashed line, respectively. For $\tau_p = 5\text{ns}$, blue-dotted line and blue-dashed-dotted line respectively illustrate \mathbb{F} and \mathbb{E} using $k = 0.5$. It deserves to emphasize the versatile potential of spectral shaping technique with which one can essentially engineer $P(n, k)$ to cooperate with the input spectrum or to get desired output echo signals.

We now turn to address the issue of how to achieve $\mathbb{E} > 54\%$. In a stationary comb system, \mathbb{E} is mainly restricted by the re-absorption during phase revival and pulse propagation [27, 30]. It is therefore critical to find a way to ease the re-absorption of emitted photons. For this we invoke the dynamical splitting of NFC illustrated in Fig. 3(a). Initially, four targets are stationary. Magnetic field \vec{B} (blue upward arrows) is applied to only targets **a1** and **a2** (green cuboids) whose nuclei experience hyperfine splitting $\Delta_g + \Delta_e = ST$. Targets **a3** and **a4** (yellow cuboids) are not magnetized and contribute unperturbed resonance to NFC. Fig. 3(c) illustrates the initial absorption peaks at zero and $\pm ST$ induced by constant hyperfine splitting. Subsequently, targets **a1** and **a3** (**a2** and **a4**) are backward (forward) accelerated and experience corresponding time-dependent Doppler shift $\Delta_D^a(t)$. The total energy shift results from both mechanical acceleration and magnetic field, namely, hybrid shift, is described by $\Delta_{31} = \Delta_g + \Delta_e + \Delta_D^a(t)$ and $\Delta_{42} = -(\Delta_g + \Delta_e) + \Delta_D^a(t)$, where $\Delta_D^a(t) = 0.5\epsilon ST \{1 + \tanh[(t - \tau_d) / (0.25b_d)]\}$. Here b_d describes the raising time of the target velocity and τ_d is the middle time of the acceleration. $\epsilon = -1, 0$, or 1 respectively depicts the forward acceleration (red Doppler shift), stationary or backward acceleration (blue Doppler shift). For a given comb spacing $S\Gamma$, the terminal velocity of an accelerated target $v = cS\Gamma/\omega$ where ω is the unperturbed transition angular frequency, and during the period of $[\tau_d - b_d/2, \tau_d + b_d/2]$ a NFC tooth at $m\Gamma$ is moving to $(m + \epsilon)\Gamma$. Fig. 3(d) depicts the NFC evolution due to above-mentioned time sequence. The contributors to each line are labelled, e.g., the top green-dashed-bent-upward line is given by target **a1** in Fig. 3(a) and by target **b1** in Fig. 3(b). Each NFC line splitting originates from a corresponding pair of targets under opposite acceleration. Alternatively, as illustrated in Fig. 3(b), one can invoke pure mechanical motion with $\Delta_{31} = \Delta_{42} = \Delta_D + \Delta_D^a(t)$ to equivalently construct above dynamical splitting of NFC. Δ_D is given by the initial velocity of each target, and $\Delta_D^a(t)$ is also introduced by acceleration. Green, orange and yellow cuboid respectively demonstrate target with $\Delta_D = ST$, $-ST$ and zero.

Three purposes of utilizing $\Delta_D^a(t)$ are (i) the absorption of the incident pulse can be enhanced by the part of comb teeth drifting inward the central resonant line; (ii) the comb is modulated so that the re-absorption condition is avoided during the whole emission process because emitters become off-resonant to re-absorbers due to time-dependent Doppler shift. Also, the input photons are distributed in different target depending on their frequency. The dynamical comb is

therefore an analogy to gradient echo memory (GEM) [32]; (iii) the frequency crossing at around $t = 60\text{ns}$ corresponds to the reversing of the spatial gradient and causes the echo emission [32]. With the numerical solution of Eq. (1-3) (see Supplementary Material for numerical method), Fig. 3(e) demonstrates the echo signal due to above dynamical NFC system illustrated in Fig. 3(d). An optimization of $\Delta_D^a(t)$ shows that \mathbb{E} is significantly raised to 67% with $\mathbb{F} = 96\%$ for an input 7ns pulse (green-dashed-filled line) when using $(\tau_d, b_d) = (60\text{ns}, 100\text{ns})$. Four cases are presented by red-solid-filled line for hybrid shift and $M = 6$ [six targets with

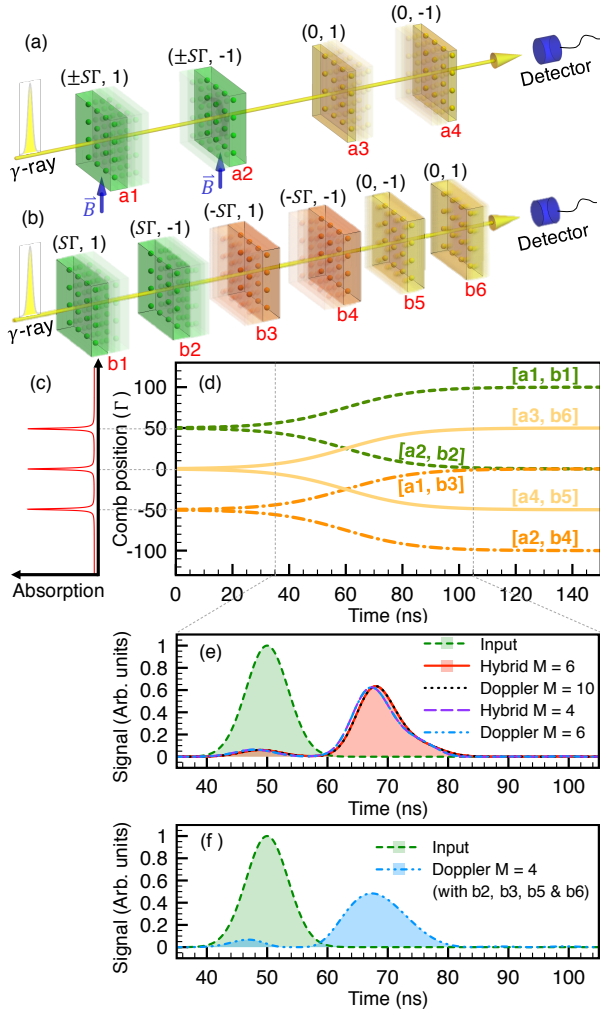


FIG. 3: (Color online) dynamical nuclear frequency comb system undergoes (a) hybrid shift (hyperfine splitting and Doppler shift) and (b) pure Doppler shift. Blue upward arrows illustrate applied magnetic fields \vec{B} , and coloured cuboids with afterimage demonstrate accelerated targets, which result in (c) initial comb and (d) dynamical splitting of nuclear frequency comb due to acceleration. (e) dynamical-comb-improved echo efficiency of 67% for an input 7ns γ -ray pulse (green-dashed-filled line). Red-solid-filled, black-dotted, purple-long-dashed and blue-short-dashed-dotted-dotted line respectively depict targets with hybrid shift for $M = 6$, pure Doppler shift for $M = 10$, hybrid shift for $M = 4$, and pure Doppler shift for $M = 6$. (f) echo efficiency of 66% due to pure Doppler shift for $M = 4$ with only targets **b2**, **b3**, **b5** and **b6**. Above each target, $(\pm\Delta_g \pm \Delta_e, \epsilon)$ is labelled in (a), and (Δ_D, ϵ) in (b).

$(\Delta_g + \Delta_e, \epsilon) = (2S\Gamma, 1), (2S\Gamma, -1), (S\Gamma, 1), (S\Gamma, -1), (0, 1)$ and $(0, -1)$]; by black-dotted line for Doppler shift and $M = 10$ [ten targets with $(\Delta_D, \epsilon) = (2S\Gamma, -1), (2S\Gamma, 1), (-2S\Gamma, -1), (-2S\Gamma, 1), (S\Gamma, -1), (S\Gamma, 1), (-S\Gamma, -1), (-S\Gamma, 1), (0, -1)$ and $(0, 1)$]; by purple-long-dashed line for hybrid shift and $M = 4$ illustrated in Fig. 3(a); by blue-short-dashed-dotted-dotted line for Doppler shift and $M = 6$ depicted in Fig. 3(b). Other parameters are $(\tau_p, S, k, v) = (7\text{ns}, 50, 0, 4.83\text{mm/s})$, $\bar{\xi} = 11.2$ for hybrid shift and $\bar{\xi} = 5.6$ for pure Doppler shift. One can perceive the equivalence of two systems by seeing the coincidence of both echo signals. We also use a 5ns pulse as an input and obtain $\mathbb{E} = 65\%$ and $\mathbb{F} = 87\%$. In the light of above purpose (iii) and Fig. 3(d), target **b1** and **b4** should contribute very limited fraction to the echo. As depicted in Fig. 3(f), we remove target **b1** and **b4** from the system of Fig. 3(b) and get an echo signal with $\mathbb{E} = 66\%$ and $\mathbb{F} = 95\%$ for a 7ns input pulse, which is very close to what we show in Fig. 3(e). Fig. 4 shows the comparison of $\bar{\xi}$ -dependent \mathbb{E} and \mathbb{F} between with and without target **b1** and **b4** in Fig. 3(b). The consistency suggests the analogy between our dynamical comb and GEM. However, its inhomogeneous energy broadening is implemented by temporal variation rather than by only spatial gradient. This distinction allows dynamical splitting scheme using only few targets to achieve $\mathbb{E} > 54\%$ comparing to our previous proposal of stepwise GEM [27], and significantly reduces the complexity of implementation. The dynamical splitting method can be applied to other wavelength region and provides a general way to achieve higher echo efficiency than the theoretical maximum [27, 30]. As depicted in Fig. 3(d), each target is accelerated to few mm/s within 100ns for the implementation of the present scheme. This is feasible [27] because reversing velocity in an even shorter interval of about 10ns had been demonstrated [28, 43–45]. Moreover, controllable few ns γ -ray source generating incident pulse had been demonstrated [17] and proposed [23].

In conclusion we have demonstrated two types of spectral control over γ -ray echo, which break the theoretical maximum echo efficiency of 54% [27, 30]. Our results lay the foundation of developing γ -ray photon memory in 10keV regime [27]. The present scheme also suggests a γ -ray echo device providing tunable time delay, which is typically difficult by

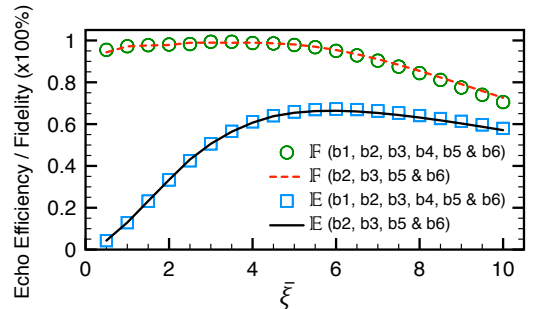


FIG. 4: (Color online) comparison of γ -ray echo between with and without target **b1** and **b4** in Fig. 3(b). Blue squares and black solid line (green circles and red-dashed line) illustrate efficiency \mathbb{E} (fidelity \mathbb{F}) with and without target **b1** and **b4**, respectively.

using exquisite γ -ray optics.

C.-J. Y., P.-H. Lin and W.-T. L. are supported by the Ministry of Science and Technology, Taiwan (Grant No. MOST 107-2112-M-008-007-MY3 and Grant No. MOST 107-2745-M-007-001-). W.-T. L. is also supported by the National Center for Theoretical Sciences, Taiwan.

* Electronic address: wente.liao@gnu.edu.tw

- [1] B. W. Adams, C. Buth, S. M. Cavaletto, J. Evers, Z. Harman, C. H. Keitel, A. Pálffy, A. Picón, R. Röhlsberger, Y. Rostovtsev, et al., *Journal of modern optics* **60**, 2 (2013).
- [2] U. van Bürck, R. L. Mössbauer, E. Gerdau, R. Ruffer, R. Hölzl, G. V. Smirnov, and J. P. Hannon, *Phys. Rev. Lett.* **59**, 355 (1987).
- [3] O. Kocharovskaya, R. Kolesov, and Y. Rostovtsev, *Phys. Rev. Lett.* **82**, 3593 (1999).
- [4] E. Kuznetsova, R. Kolesov, and O. Kocharovskaya, *Phys. Rev. A* **68**, 043825 (2003).
- [5] T. J. Bürvenich, J. Evers, and C. H. Keitel, *Phys. Rev. Lett.* **96**, 142501 (2006).
- [6] F. Vagizov, R. Manapov, E. Sadykov, V. Lyubimov, and O. Kocharovskaya, *Hyperfine Interactions* **188**, 143 (2009).
- [7] R. Röhlsberger, K. Schlage, B. Sahoo, S. Couet, and R. Ruffer, *Science* **328**, 1248 (2010).
- [8] W.-T. Liao, A. Pálffy, and C. H. Keitel, *Physics Letters B* **705**, 134 (2011).
- [9] R. Röhlsberger, H. C. Wille, K. Schlage, and B. Sahoo, *Nature* **482**, 199 (2012).
- [10] W.-T. Liao, A. Pálffy, and C. H. Keitel, *Phys. Rev. C* **87**, 054609 (2013).
- [11] K. P. Heeg, H.-C. Wille, K. Schlage, T. Guryeva, D. Schumacher, I. Uschmann, K. S. Schulze, B. Marx, T. Kämpfer, G. G. Paulus, et al., *Phys. Rev. Lett.* **111**, 073601 (2013).
- [12] K. P. Heeg, J. Haber, D. Schumacher, L. Bocklage, H.-C. Wille, K. S. Schulze, R. Loetzsch, I. Uschmann, G. G. Paulus, R. Ruffer, et al., *Phys. Rev. Lett.* **114**, 203601 (2015).
- [13] Y. V. Radeonychev, V. A. Antonov, F. G. Vagizov, R. N. Shakhmuratov, and O. Kocharovskaya, *Phys. Rev. A* **92**, 043808 (2015).
- [14] W.-T. Liao, C. H. Keitel, and A. Pálffy, *Scientific reports* **6**, 33361 (2016).
- [15] J. Haber, X. Kong, C. Strohm, S. Willing, J. Gollwitzer, L. Bocklage, R. Ruffer, A. Pálffy, and R. Röhlsberger, *Nature Photonics* **11**, 720 (2017).
- [16] I. R. Khairulin, V. A. Antonov, Y. V. Radeonychev, and O. Kocharovskaya, *Phys. Rev. A* **98**, 043860 (2018).
- [17] F. Vagizov, V. Antonov, Y. Radeonychev, R. Shakhmuratov, and O. Kocharovskaya, *Nature* **508**, 80 (2014).
- [18] W.-T. Liao and A. Pálffy, *Phys. Rev. Lett.* **112**, 057401 (2014).
- [19] W.-T. Liao and S. Ahrens, *Nature Photon.* **9**, 169 (2015).
- [20] K. P. Heeg, C. Ott, D. Schumacher, H.-C. Wille, R. Röhlsberger, T. Pfeifer, and J. Evers, *Phys. Rev. Lett.* **114**, 207401 (2015).
- [21] K. P. Heeg, A. Kaldun, C. Strohm, P. Reiser, C. Ott, R. Subramanian, D. Lentrodt, J. Haber, H.-C. Wille, S. Goertler, et al., *Science* **357**, 375 (2017).
- [22] W.-T. Liao and A. Pálffy, *Scientific Reports* **7**, 321 (2017).
- [23] G.-Y. Wang and W.-T. Liao, *Phys. Rev. Applied* **10**, 014003 (2018).
- [24] W.-T. Liao, A. Pálffy, and C. H. Keitel, *Phys. Rev. Lett.* **109**, 197403 (2012).
- [25] Y. V. Shvyd'ko, T. Hertrich, U. van Bürck, E. Gerdau, O. Lepold, J. Metge, H. D. Rüter, S. Schwendy, G. V. Smirnov, W. Potzel, et al., *Phys. Rev. Lett.* **77**, 3232 (1996).
- [26] X. Kong and A. Pálffy, *Phys. Rev. Lett.* **116**, 197402 (2016).
- [27] X. Zhang, W.-T. Liao, A. Kalachev, R. Shakhmuratov, M. Scully, and O. Kocharovskaya, *arXiv preprint arXiv:1812.11441* (2018).
- [28] P. Heliö, I. Tittonen, M. Lippmaa, and T. Katila, *Phys. Rev. Lett.* **66**, 2037 (1991).
- [29] P. Heliö and I. Tittonen, *Hyperfine interactions* **135**, 167 (2001).
- [30] N. Sangouard, C. Simon, M. Afzelius, and N. Gisin, *Phys. Rev. A* **75**, 032327 (2007).
- [31] S. A. Moiseev and N. M. Arslanov, *Phys. Rev. A* **78**, 023803 (2008).
- [32] G. Hétet, J. J. Longdell, M. J. Sellars, P. K. Lam, and B. C. Buchler, *Phys. Rev. Lett.* **101**, 203601 (2008).
- [33] W. Tittel, M. Afzelius, T. Chaneliere, R. L. Cone, S. Kröll, S. A. Moiseev, and M. Sellars, *Laser & Photonics Reviews* **4**, 244 (2010).
- [34] X. Zhang, A. Kalachev, and O. Kocharovskaya, *Phys. Rev. A* **90**, 052322 (2014).
- [35] W.-T. Liao, C. H. Keitel, and A. Pálffy, *Phys. Rev. Lett.* **113**, 123602 (2014).
- [36] S.-W. Su, S.-C. Gou, L. Y. Chew, Y.-Y. Chang, I. A. Yu, A. Kalachev, and W.-T. Liao, *Phys. Rev. A* **95**, 061805 (2017).
- [37] M. Afzelius, C. Simon, H. de Riedmatten, and N. Gisin, *Phys. Rev. A* **79**, 052329 (2009).
- [38] Z.-Q. Zhou, W.-B. Lin, M. Yang, C.-F. Li, and G.-C. Guo, *Phys. Rev. Lett.* **108**, 190505 (2012).
- [39] M. O. Scully and M. S. Zubairy, *Quantum Optics* (Cambridge University Press, 2006).
- [40] X. Kong, W.-T. Liao, and A. Pálffy, *New Journal of Physics* **16**, 013049 (2014).
- [41] X. Zhang, A. Kalachev, P. Hemmer, and O. Kocharovskaya, *arXiv preprint arXiv:1602.02322* (2016).
- [42] Y.-H. Chen, M.-J. Lee, I.-C. Wang, S. Du, Y.-F. Chen, Y.-C. Chen, and I. A. Yu, *Phys. Rev. Lett.* **110**, 083601 (2013).
- [43] I. Tittonen, M. Lippmaa, P. Heliö, and T. Katila, *Phys. Rev. B* **47**, 7840 (1993).
- [44] R. N. Shakhmuratov, F. Vagizov, and O. Kocharovskaya, *Phys. Rev. A* **84**, 043820 (2011).
- [45] R. N. Shakhmuratov, F. Vagizov, and O. Kocharovskaya, *Phys. Rev. A* **87**, 013807 (2013).